Available online at www.sciencedirect.com

ScienceDirect

Geochimica et Cosmochimica Acta 204 (2017) 252–266

Geochimica et Cosmochimica Acta

www.elsevier.com/locate/gca

Spatially-variable carbonation reactions in polycrystalline olivine

Rachel K. Wells [a,*], Wei Xiong [b], Erika Sesti [c], Jinlei Cui [c], Daniel Giammar [b], Philip Skemer [a], Sophia E. Hayes [c], Mark S. Conradi [c,d]

[a] Department of Earth & Planetary Sciences, Washington University in St. Louis, Campus Box 1190, One Brookings Drive, St. Louis, MO 63130, United States

[b] Department of Energy, Environmental and Chemical Engineering, Washington University in St. Louis, Campus Box 1180, One Brookings Drive, St. Louis, MO 63130, United States

[c] Department of Chemistry, Washington University in St. Louis, Campus Box 1134, One Brookings Drive, St. Louis, MO 63130, United States

[d] Department of Physics, Washington University in St. Louis, Campus Box 1105, One Brookings Drive, St. Louis, MO 63130, United States

Received 18 October 2016; accepted in revised form 2 February 2017; Available online 11 February 2017

Abstract

Carbon dioxide (CO_2) injection into olivine-rich mafic and ultramafic rocks is expected to result in the precipitation of divalent metal carbonate minerals, permanently storing the CO_2 underground. Previous experiments that used unconsolidated forsterite (Mg_2SiO_4) particles in experimental investigations of reactions with water and carbon dioxide have been useful for determining the identity, rates of formation, and spatial location of carbonate mineral reaction products. However there remains a need for information regarding the influence of the internal pore structure and grain boundary surfaces on the extent and locations of these reactions in dense aggregates. We conducted several experiments at 100 °C and 100 bar CO_2 using sintered San Carlos olivine (Fo_{90}) and pure forsterite (Fo_{100}) cylinders, and we documented the type and spatial distribution of the reaction products. Timing of carbonation was measured using in-situ ^{13}C NMR spectroscopy without removing the sample from the reactor. Ex-situ solid-state NMR spectroscopy, Raman spectroscopy, and electron microscopy were used to examine reacted samples and precipitates. Within 15 days, magnesite is observed only on the surface of Fo_{90}. After 53 and 102 days of reaction, magnesite and amorphous silica are observed as a crust around the entire Fo_{100} cylinder and as isolated layers within the sample. The spatial transition from an amorphous silica layer to the host Fo_{100} indicates that the development of amorphous silica did not impede further forsterite dissolution. While earlier studies documented localized reactions at the grain scale, the development of distinct zones of magnesite and amorphous silica suggest that divalent metal cations are mobile during carbonation of olivine. Grain boundaries, pore structure, and geochemical gradients strongly influence the locations of silicate mineral dissolution and carbonate mineral precipitation even in the absence of advective transport or confinement. The clear spatial distribution of precipitates observed in this study indicates that carbonation in heterogeneous reservoirs may be strongly affected by grain-scale microstructure.

Keywords: Carbon sequestration; Olivine; Magnesite precipitation

1. INTRODUCTION

Amongst the various CO_2-rock reactions that have been proposed for geological carbon sequestration, olivine-rich rocks offer the greatest promise for mineral trapping due to olivine's fast dissolution rate under acidic conditions and abundance of divalent metals that are needed to form carbonate minerals (IPCC, 2005; Oelkers et al., 2008; Matter and Kelemen, 2009; Kelemen et al., 2011; Gislason and Oelkers, 2014). Basalt is an especially favorable target for CO_2 sequestration because it often contains

* Corresponding author.
E-mail address: rwells@wustl.edu (R.K. Wells).

http://dx.doi.org/10.1016/j.gca.2017.02.003
0016-7037/

both olivine and divalent metal-rich pyroxene-group minerals and is also widely abundant at or near Earth's surface (Lackner et al., 1995; Kelemen and Matter, 2008; Oelkers et al., 2008; Goldberg and Slagle, 2009; Krevor et al., 2009; Schaef et al., 2010). Indeed, sequestration of CO_2 in basalt has already been implemented successfully in two pilot experiments (Big Sky Carbon Sequestration Project pilot well in Washington, USA (McGrail et al., 2017), and CarbFix pilot well in Iceland (Matter et al., 2016)).

The carbonation reaction for olivine:

$$(X)_2SiO_4(\text{Olivine}) + 2CO_2 = 2(X)CO_3(\text{Carbonate}) + SiO_2 \quad (1)$$

where X is Mg and/or Fe, indicates that the primary products are projected to be the carbonates magnesite ($MgCO_3$) and/or siderite ($FeCO_3$), and silicon dioxide (Kelemen and Matter, 2008). The formation of quartz is not expected at the temperatures involved in geologic carbon sequestration; rather, amorphous silica is typically observed (Daval et al., 2011; Cui et al., 2016). If Ca-rich pyroxene is also present, as is often the case for peridotites and crystalline basalts, the carbonation reaction:

$$CaMgSi_2O_6(\text{Pyroxene}) + 2CO_2 = CaCO_3(\text{Calcite}) + MgCO_3(\text{Magnesite}) + 2SiO_2, \quad (2)$$

indicates that calcite ($CaCO_3$) may precipitate in addition to magnesite and siderite (Kelemen and Matter, 2008; Gudbrandsson et al., 2011). The observation of carbonate veins within peridotite formations suggests that carbonation reactions occur naturally (Matter and Kelemen, 2009). Initial investigations of an active carbon storage well in Iceland (CarbFix pilot well in fractured and porous basalt) observed calcite less than two years after injection (Matter et al., 2016). Ankerite (Fe-bearing calcite) precipitates were recently reported in a carbon sequestration test well into fractured basalt in eastern Washington state two years after injection (McGrail et al., 2017).

Evidence from short-term bench-scale experiments with olivine in aqueous CO_2 suggest that the development of carbonate minerals can occur within two weeks at elevated experimental temperatures of 50–185 °C (Giammar et al., 2005, 2014; Kim et al., 2005; Béarat et al., 2006; Kwak et al., 2010, 2011; Daval et al., 2011; Kwon et al., 2011; Felmy et al., 2012; Qafoku et al., 2012, 2014; Surface et al., 2013; Xiong and Giammar, 2014; Peuble et al., 2015). The carbonate minerals that do form are usually small magnesite crystals, particularly when the experiments used as reactants the forsterite (Fo_{100}) endmember of the olivine solid solution (Mg_2SiO_4) (Giammar et al., 2005; Kwon et al., 2011; Felmy et al., 2012; Surface et al., 2013; Qafoku et al., 2014; Xiong and Giammar, 2014; Moore et al., 2015) or siderite crystals, if Fe-rich silicates are reacted (Felmy et al., 2012). However, hydrated minerals such as nesquehonite ($Mg(HCO_3)(OH)\cdot 2(H_2O)$) and hydromagnesite ($Mg_5(CO_3)_4(OH)_2\cdot 4H_2O$) may precipitate more readily than magnesite at low temperatures (<100 °C) and pressures (Davies and Bubela, 1973; Hänchen et al., 2008; Qafoku et al., 2014). Amorphous silica is often documented as a nanometer-scale layer across the surface of single forsterite grains (Béarat et al., 2006; Davis et al., 2009; Jarvis et al., 2009; Daval et al., 2011; Kwak et al., 2011; Cui et al., 2016). This layer may become impermeable as reactions progress and limit interaction between CO_2 and forsterite (Béarat et al., 2006; Andreani et al., 2009; Jarvis et al., 2009; Wang and Giammar, 2013). However, Daval et al. (2011) suggest that an amorphous silica layer may not interfere with the olivine carbonation depending on specific conditions (e.g., surface characteristics, temperature, pressure) at the time of reaction.

Most of these bench-scale experiments used individual olivine grains or un-compacted particles to increase the surface area of the reactant and hence the potential for carbonate mineral formation. While this is an effective method for laboratory-based experiments focused on the rates and products of the chemical reactions, large-scale carbon sequestration initiatives are in natural geologic formations, such as the Columbia River flood basalt (McGrail et al., 2011; Zakharova et al., 2012) and Icelandic basalt. These formations are composed of consolidated grains that joined during crystallization, and the resulting porosity can have a large range (0–0.5) (Franzson et al., 2008; Zakharova et al., 2012). Packed bed experiments with particles (Surface et al., 2013; Giammar et al., 2014; Xiong and Giammar, 2014; Moore et al., 2015) partially simulate natural rocks with a porosity of 0.4–0.5, and an interconnected pore network. With this added pore structure, precipitates exhibited a spatial pattern in relation to the length of the sample (Xiong and Giammar, 2014). A limited number of studies observed evidence for localized dissolution and precipitation in batch and flow-through experiments with solid rock including peridotite (Andreani et al., 2009; Hövelmann et al., 2011, 2012; van Noort et al., 2013) and experimentally sintered olivine (Peuble et al., 2015). Olivine grains with irregular surfaces and amorphous silica layers were more common in areas of high flow rate (Andreani et al., 2009). Carbonate precipitation was more common in pre-existing fractures (Hövelmann et al., 2012) or pores (van Noort et al., 2013; Peuble et al., 2015) and in zones with little to no flow (Andreani et al., 2009).

This study focuses on the spatial and geochemical interaction between Fo_{90} and Fo_{100} olivine and CO_2-rich fluids using vacuum-sintered olivine samples. The vacuum-sintering process creates denser samples with fused grain boundaries, which will be more similar to natural reservoir structures than previous packed bed experiments, while providing a simplified chemistry that is not afforded by experiments on natural samples. The objectives of this study were to observe the timing of precipitation, characterize the composition of the precipitates, and determine their spatial distribution across the samples. We reacted sintered olivine cylinders with different geometries in water at 100 °C equilibrated with 100 bar CO_2 for up to 102 days. Post-reaction samples were characterized using optical and electron microscopy, Raman spectroscopy, and ex-situ solid-state nuclear magnetic resonance (NMR) spectroscopy. The experimental observations indicate that the overall surface geometry of each sintered sample does not undergo a significant change, while the dissolution and precipitation processes are strongly segregated into specific sections of the samples.

2. METHODS

2.1. Synthesis of starting materials

All experimental samples were synthesized from olivine powders. One set of samples was synthesized from pure synthetic forsterite powder (Fo_{100}) (Mg_2SiO_4; 99% purity; Alfa Aesar), which was sieved to yield particles smaller than 44 μm. The Mg-endmember of olivine was required for the NMR experiments as large concentrations of iron might interfere with the collection of NMR spectra. A second set of samples was synthesized from natural, iron-bearing San Carlos olivine (Fo_{90}) ($Mg_{0.9}Fe_{0.1}SiO_4$). In this case, single crystals of optically clear olivine were separated from ultramafic xenoliths from the San Carlos volcanic field. Olivine grains were crushed in an agate mortar and pestle under water, mechanically milled using an agate ball mill, and sieved to a final grain size of less than 53 μm. Forsterite and olivine powders were used without any further processing.

The powders were pressed and vacuum-sintered following established procedures (e.g., Gribb and Cooper, 1998). Cylindrical pellets were made with 6 mm and 13 mm diameter die molds. The initial porosity of the cold pressed pellets was greater than 0.30, which was calculated by comparing the starting density of the pellet to the theoretical density of olivine. Each pellet was then vacuum-sintered at 1300 °C for 48 h at a vacuum of less than 10^{-5} Torr. At these conditions, no evidence of grain growth was observed. This process results in sintered grain contacts and a decrease in porosity to approximately 0.25. While many of the grain boundaries are sintered, the some of the remaining pores may still be interconnected.

We used two geometries to observe carbonation, one with solid (s) cylinders and one with saw-cut (f) cylinders (Fig. 1; Table 1). Solid sample geometries (Fo90_s1, Fo90_s2, and Fo100_s) were left unaltered following vacuum-sintering. Two cylinders (Fo90_f and Fo100_f) were cut in half using a diamond blade rotary saw to simulate a fracture. The fracture orientation for the Fo_{90} sample was made perpendicular to the length of the cylinder, while the Fo_{100} sample was oriented vertically. Each fracture opening is approximately 1 mm as measured using optical microscopy.

2.2. Fo_{90} experiments

Two different geometries were tested using a high pressure vessel (Parr Instrument, 300 mL stainless steel vessel) (Fig. 1; Table 1). One experiment included two single cylindrical samples (each 1 cm in length) (Fo90_s1 and Fo90_s2) stacked end to end. The two samples were joined together with rubber tubing, with the top exposed and the bottom blocked by a short glass rod with the same diameter as the sintered cores (Fig. 1A). This setup creates fracture-like openings between the first and second sample and between the outside of the samples and the rubber tubing. We devised another setup that included a single sintered olivine pellet (1 cm in length) (Fo90_f) with a saw cut oriented perpendicular to the vertical axis of the cylinder in the center of the sample. Unlike the fracture-like opening in the stacked experiment, the simulated fracture has a different roughness than that of the end sections and cylindrical sides. This sample was also assembled in rubber tubing with a glass stopper on the end and the top exposed to limit the pathways for fluid transport (Fig. 1A).

Each assembly was vertically fixed to tubing that is attached to the reactor head, and then placed in a 300-mL pressure vessel with a PTFE liner. Ultrapure water (200 mL) (resistivity >18.2 MΩ-cm) was added so that the samples were entirely immersed. After the vessel head was assembled, the sample was heated and then a syringe pump (500D, Teledyne Isco) provided a constant CO_2 pressure (100 bar) on the headspace, with 1% air remaining. The pressure stabilized within 1 h, indicating the water was at equilibrium with the CO_2. The entire vessel was maintained at 100 °C by a heating mantle, and the stirring speed was set at 60 rpm. These Fo_{90} samples were reacted for 15 days. At the end each experiment, the heating mantle was removed and the vessel was allowed to cool to room temperature. The remaining pressure was allowed to bleed off over several hours. Samples were removed from the vessel and allowed to air-dry at room temperature. Precipitates were observed on the surface of the sample before drying.

2.3. Fo_{100} experiments

All Fo_{100} samples were reacted in an in-situ NMR probe suitable for gases, liquids, and solids, which is a batch style probe with a pressure-containing ceramic sample holder (Fig. 1B). Air within the headspace was evacuated. Elevated pressure ^{13}C-enriched CO_2 gas (99% purity from Sigma Aldrich) was loaded into a small volume vessel attached to the manifold, and then released into the probe at a pressure of 100 bar. Fo_{100} cylinders were submerged in 2 mL of ultrapure water (resistivity >18.2 MΩ-cm) and then heated to a constant temperature of 100 °C. More information on the details of the probe and high-pressure manifold to which it is coupled, as well as its operation, can be found in Surface et al. (2013) and Moore et al. (2015). The pressure was observed to be stable within 1 h. ^{13}C NMR experiments were conducted at a Larmor frequency of 89.07 MHz with no ^1H decoupling. The spectra were referenced using the CO_2 (g) peak at 128.6 ppm for these experimental conditions (Surface et al., 2013). At the end of each experiment, the vessel was cooled to room temperature over 1–2 h, and any remaining labeled CO_2 was collected, bringing the vessel back to atmosphere.

Experiments were conducted in two different modes. For the Fo_{100} NMR experiment (Fo100_s), the reaction was monitored over a period of 102 days using a Bloch decay ("1-pulse" sequence). Instead of holding the sample with rubber tubing, the single cylinder was placed on a spacer[1]

[1] Two different spacers were used for two separate experiments. Glass wool was used for sample Fo100_s, and a piece of zirconia was used for sample Fo100_f. The silica present in the glass wool may have acted as a trap for some CO_2; however, the resulting precipitates studied by NMR were similar, irrespective of the spacer composition.

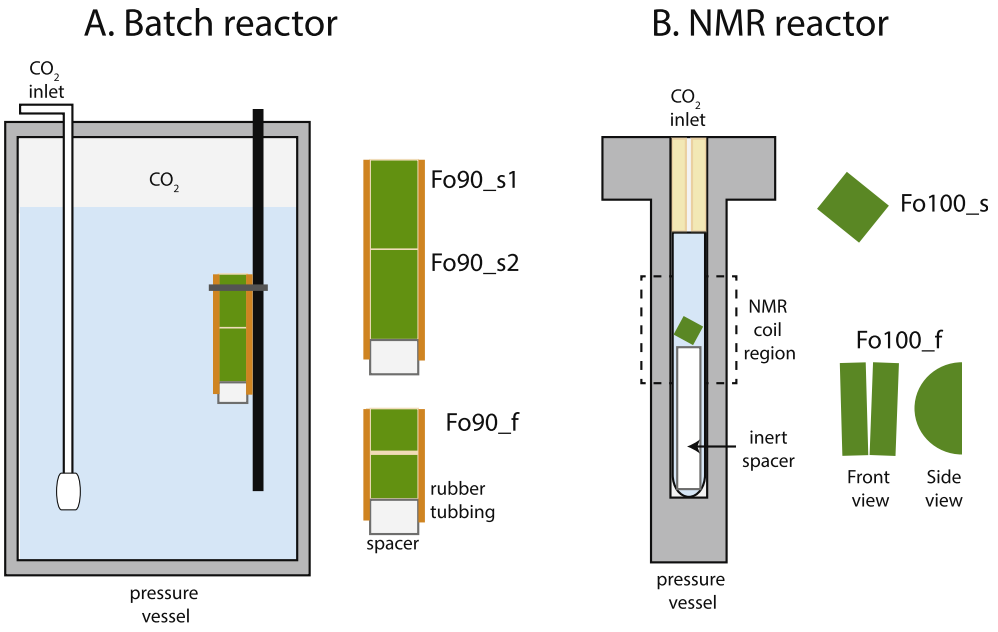

Fig. 1. Cross-section of high pressure reactors (A) 300-mL batch reactor and (B) a 2-mL in-situ ^{13}C NMR reactor, and the corresponding vacuum-sintered samples.

Table 1
Batch and in-situ NMR experiments.

Experiment	Sample ID	Geometry	Radius, Length (mm)	Mass (g)	Porosity (%)	Temperature (°C)	Starting pressure (bar)	Final pressure (bar)	H_2O volume (mL)	Reaction time (days)
1	Fo90_s1	Cylinder	3.0, 10.4	0.8	25.1	100	100	100	200	15
	Fo90_s2	Cylinder	3.0, 10.1	0.7	26.6					
2	Fo90_f	Cylinder with saw cut	3.0, 6.7	0.5	24.7	100	100	100	200	15
3	Fo100_s	Cylinder	3.0, 6.5	0.5	17.8	100	100	45	2	102
4	Fo100_f	Cylinder with saw cut	6.5, 3.7	0.9	26.9	100	100	100	2	53

(Fig. 1B). As the experiment progressed, the initial charge of 100 bar of $^{13}CO_2$ gas partially reacted, and no additional gas was added. Therefore, the pressure at the end of the experiment was 45 bar. An initial Bloch decay spectrum was collected for the first dataset (Sample Fo100_s, day 33) using an inspection pulse of 10 μs with a recycle delay of 30 s and recording 8 transients. The remaining data sets were all collected using a Bloch decay pulse sequence with an optimized π/2 pulse of 22.5 μs and a recycle delay of 30 s, recording 1028 transients.

Another Fo_{100} cylinder was cut in half, and each side was placed side-by-side to simulate a fracture. The sample was placed freestanding on a spacer. For this sample (Fo100_f), a Hahn pulse echo sequence was used for NMR, and the pressure was kept at 100 bar. The sample was monitored over a period of 53 days. For the Hahn echo pulse sequence, a typical inspection pulse was 16.85 μs, the π pulse was 33.7 μs, and a τ delay of 130 μs was used. The recycle delay was 30 s, and the number of transients recorded was 1440.

2.4. Post-reaction analysis

Each sample required some physical alteration for additional NMR and microstructural analysis. Before each sample was crushed for ex-situ NMR or sliced to produce a thin-section for microanalysis, the outer surface was analyzed using Raman spectroscopy (HoloLab Series 5000 Laser Raman Microprobe, Kaiser Optical), with a 532 nm laser and a 20× power objective that probes a 5 μm area. Fo_{90} samples (Fo90_s1, Fo90_s2, and Fo90_f) were dissected into five slices from the top in 1 mm increments. Fo_{100} samples (Fo100_s and Fo100_f) were cut into two pieces.

Ex-situ $^{13}C\{^1H\}$ magic angle spinning (MAS) and $^{13}C\{^1H\}$ static NMR spectra were acquired on a Chemagnetics 4 mm MAS triple resonance probe using a Larmor frequency of 74.18 MHz for ^{13}C. The top 2 mm of sample Fo100_s was removed and analyzed, and a 3 mm portion of the middle of the fractured Fo100_f sample, which contained a new unidentified material in the fracture, was ana-

lyzed. Static and MAS experiments were conducted using a Hahn echo sequence with π/2 pulses of 4.23 μs, π pulses of 8.46 μs, and a rotor-synchronized τ delay of 193.65 μs. For static experiments, 1440 transients were acquired, while 256 transients were recorded for MAS measurements. The ^{1}H decoupling strength for all experiments was 58.8 kHz at a ^{1}H Larmor frequency of 294.973 MHz. Typical spinning speeds for MAS experiments were ~5 kHz. All spectra were referenced to adamantane ($C_{10}H_{16}$) at 38.48 ppm.

The pH of the starting solution was calculated using charge balance for a water and CO_2 system at 100 °C and 100 bar. Equilibrium constants were determined with the program SUPCRT92, and CO_2 solubility was calculated using the model from Duan and Sun (2003). To calculate the final pH of the bulk solution, a sample of the bulk solution (Fo100_f) was taken for inductively coupled plasma mass spectrometry (ICP-MS). The concentration of Mg in the bulk solution, which was released from Fo_{100}, is added to the system calculation. Estimates of the pH for Fo100_s experiment were made using Moore et al. (2015) and Surface et al. (2015).

Analysis of precipitates on the outer surface of the Fo_{90} samples and the cross-sectional view of the Fo_{100} samples were made using optical and electron microscopy (JEOL 7001LVF FE-SEM; FEI Nova 230). Backscatter electron (BSE) and secondary electron (SE) imaging were used to document microstructures. Compositional analysis, including energy dispersive spectroscopy (EDS) and wavelength dispersive spectroscopy (WDS) of the precipitates were performed using an electron microprobe (JEOL JXA-8200). Compositions were normalized to either the number of oxygens present in forsterite or CO_3 for carbonates. Cathodoluminescence (CL) was also used to determine slight changes in composition when more than one carbonate mineral precipitated.

3. RESULTS

3.1. San Carlos olivine (Fo_{90})

3.1.1. Single cylinder experiments (Fo90_s1 and Fo90_s2)

After 15 days of reaction, we observed precipitates on the outer surface of each sample using both optical and electron microscopy (Fig. 2A). These precipitates occurred between the sample and the rubber tubing ~2–3 mm below the top of the sample that was open to the CO_2-rich aqueous solution. We also observed precipitates between the bottom of Fo90_s1 and the top of Fo90_s2 (Fig. 2B). No precipitates were observed on the top surface of Fo90_s1 or within either sample. Mg concentrations are too low for nucleation on the top surface of the sample that is exposed to the bulk solution because Mg can diffuse away from the surface into the 200 mL of solution, and the pH is also at its lowest here. The precipitates grew to a size of 5–40 μm on the surface of the samples, and are at their maximum concentration approximately 1 cm down from the top of the uppermost cylinder (Fo90_s1). Raman spectroscopy of the precipitates on the surface shows strong peaks at 1094 cm^{-1} and 330 cm^{-1}, which correspond to

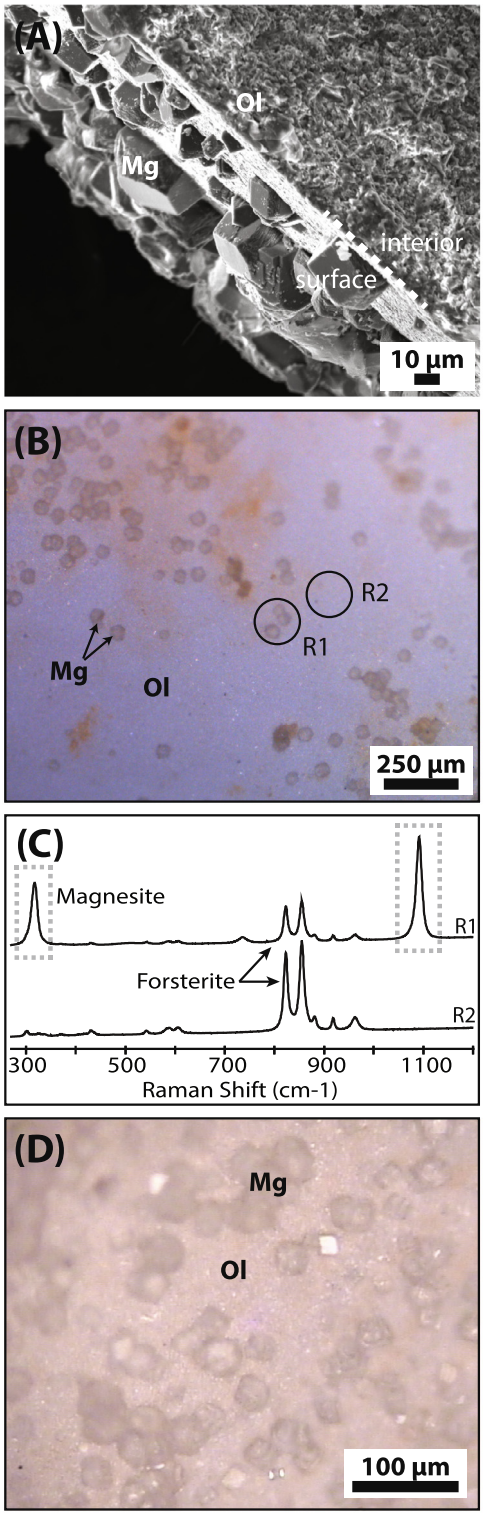

Fig. 2. San Carlos Olivine (Fo_{90}) experimental microscopy and spectroscopy results with (A) SE image of magnesite (Mg) crystals on the side of one Fo90 (Ol) cylinder (Fo90_s1), (B) optical photomicrograph of the bottom surface of Fo90_s1, which contains ~50 μm magnesite grains, (C) Raman spectra of two surface sites (R1, R2) indicating Fo_{90} (arrows) and magnesite (dashed box), and (D) optical photomicrograph of magnesite grains on the surface of the fracture (OL3_f).

the CO_3^{2-} symmetric stretching external mode (V_1) in magnesite (Fig. 2C) (Edwards et al., 2005; Boulard et al., 2012). We also analyzed the surface of the sample that had no visible precipitates. The peaks at 824, 855, and 964 cm^{-1} correspond to the stretching modes of the three types of Si–O bonds in olivine (Mohanan et al., 1993). The three olivine peaks are also observed in the magnesite spectra because the beam, which was bigger than the magnesite grain, detected both the precipitate and the host Fo_{90}. No other precipitates were observed on the surface of the samples.

3.1.2. Fractured cylinder experiment (Fo90_f)

The fractured Fo_{90} sample (Fo90_f) was also reacted for 15 days, and contains precipitates on the vertical walls of the cylinder, between the sample and the rubber tubbing, which is where we observed precipitates in the single cylinder (Fo90_s1 and Fo90_s2). Precipitates are also observed on the fracture surface (Fig. 2D). Within the horizontal fracture, the grains are 10–50 μm and do not seal the fracture opening. Raman spectroscopy confirmed that these precipitates are also magnesite. These findings are similar to what we observed in the stacked single cylinder experiments, which suggests that these results are consistent and reproducible.

3.2. Forsterite (Fo_{100})

3.2.1. Single cylinder experiment (Fo100_s)

The in-situ ^{13}C NMR data of the single cylinder sample (Fo100_s) show the growth of the carbonate mineral resonance (broad lineshape with a peak at ~190 ppm) over time (Fig. 3A). Based on previous experiments with other materials, the first data set was collected after 33 days of reaction. As the reaction progresses towards a total of 102 days of reaction, the carbonate resonance increases in area, and a carbonate chemical shift anisotropy-broadened (CSA) powder pattern becomes more apparent. The other peaks in the spectra are attributed to CO_2 (aqueous, supercritical, and gaseous) around 126 ppm and dissolved bicarbonate ($HCO_{3-(aq)}$) at 161 ppm. The bicarbonate peak intensity at 161 ppm changes with time, reflecting the changing pH inside the reaction chamber. The pH of the solution in the reactor is estimated to increase from 3.2 to 5.5 based on the $[^{13}CO_2]/[H^{13}CO_3^-]$ ratios described in Moore et al. (2015) and Surface et al. (2015). Following reaction, the sample was observed to be tilted at ~45° within the glass tube (i.e., the sample's long axis was no longer parallel with the glass tube). For post-reaction analysis, the sample was cut in half along the vertical axis for ex-situ $^{13}C\{^1H\}$ NMR analysis and microscopic analysis. The segment designated for additional NMR analysis was then cut into two pieces, with the primary analysis coming from a 2 mm slice off the top of this segment, which contained the most visible precipitates.

Ex-situ $^{13}C\{^1H\}$ NMR analysis of the top 2 mm slice displays a CSA powder pattern that is consistent with the magnesite endmember ($\eta = 0.14$, $\delta_{aniso} = -54.5$ ppm) (Fig. 3B) similar to what has been shown previously (Feng, 2009; Moore et al., 2015). A ^{13}C magic angle spinning (MAS) spectrum was collected on this same sample, and the 169.5 ppm isotropic resonance was found, consistent with $MgCO_3$ (Fig. 3C) (Moore et al., 2015). Fig. 3B indicates that there is only a single resonance present and only one carbon site (Moore et al., 2015). Due to the small amount of sample, Teflon spacers were used to center the sample into the coil region, and as a result, a Teflon carbon resonance at 111 ppm can also be seen in the MAS spectrum (Fig. 3B). The Teflon resonance is not visible in the static spectrum both because it is outside the coil region and because the broad magnesite powder pattern likely obscures it. When the sample was removed from the probe, we noted that the water volume had decreased though the

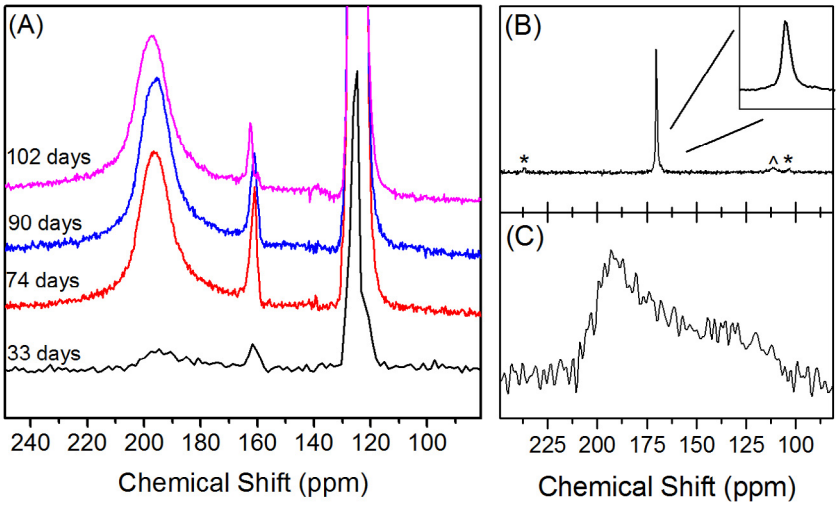

Fig. 3. (A) in-situ static ^{13}C NMR of the Fo_{100} (Fo100_s) reaction. The carbonate mineral chemical shift anisotropy (CSA) powder pattern dominated by a peak at approximately 190 ppm grows in with reaction time. The resonance at 161 ppm is bicarbonate, and the peaks around 126 ppm are various CO_2 phases. (B) and (C) are the ex-situ $^{13}C\{^1H\}$ MAS and static NMR, respectively, of the top portion of the sample. The MAS spectrum (B) is a single resonance at 170.2 ppm (inset) with spinning side bands marked with (*). Teflon spacers were used resulting in the resonance at 111 ppm marked with (^). The static $^{13}C\{^1H\}$ powder pattern of the Fo_{100} sample is shown in (C).

sample remained submerged, and the orientation of the sample was tilted at a ~45°. For microstructural and compositional analysis, we marked the orientation on the thin section.

Precipitation across the exterior surface of the sample was not evenly distributed (Fig. 4). Large globular mounds (1 mm wide) composed of fine crystals (<5 μm) occur on the top surface (located closest to the CO_2-water interface) (Fig. 4A and B), while we only observe small individual crystals (1–5 μm) on the vertical and bottom surfaces of the sample. The overall size and shape of the sample remained approximately the same.

Cross-sectional analysis (Figs. 4A and 5) of the sample indicates that magnesite surrounds the entire surface of

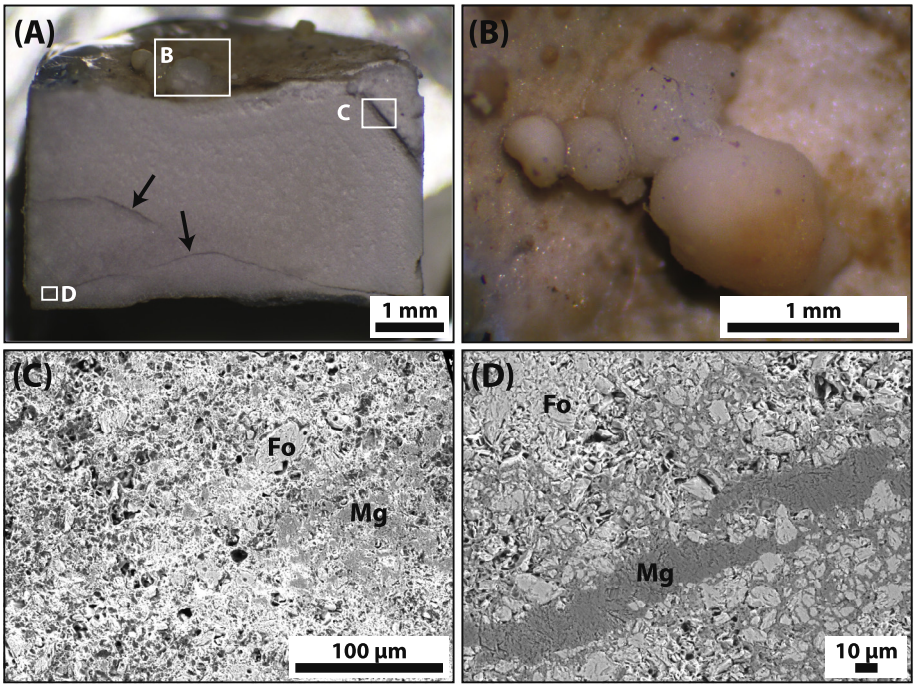

Fig. 4. Single Fo_{100} sample (Fo100_s) microstructures showing (A) an optical photomicrograph of the cross-section of magnesite-encrusted Fo_{100} core with two magnesite-filled veins (arrows) within the sample, (B) an optical photomicrograph of magnesite formed in globular mounds (<1 mm wide) on top of the sample, (C) a BSE image of amorphous silica (dark grains with bright grain boundaries) surrounding Fo_{100} (Fo) and magnesite (Mg) grains, and (D) a BSE image of magnesite precipitated within a pre-existing fracture and into the fracture wall.

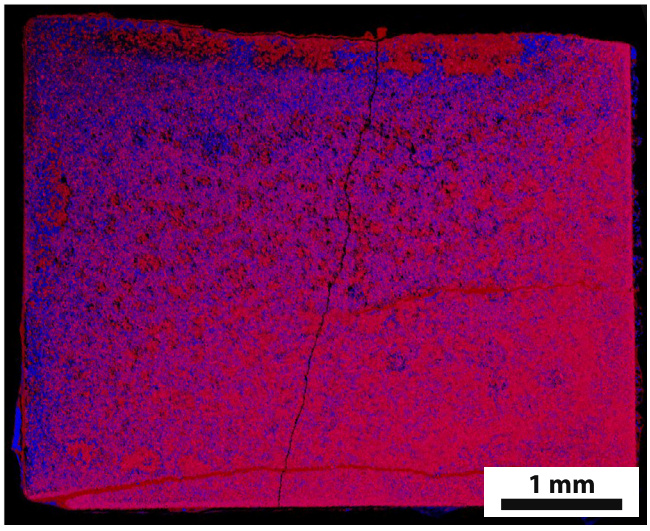

Fig. 5. Single Fo_{100} sample (Fo100_s) EDS map. The final orientation of the sample with respect to the CO_2 inlet is shown in Fig. 1. Transitions from amorphous silica (purple-blue) to Fo_{100} (pink). Magnesite (red) is more common in the Fo_{100}-rich areas. Mg-red, Si-blue. (For interpretation of the references to colour in this figure legend, the reader is referred to the web version of this article.)

the cylinder, and a transition from forsterite and magnesite (lower portion of the sample) to amorphous silica (upper portion of the sample) occurs within the cylinder. In addition to the globular mound of magnesite on the top surface of the sample, the vertical sides and bottom surface are rimmed by a ~8 μm thick crust of magnesite. Magnesite also occurs as veins within the sample, which formed along pre-existing fractures created during sample preparation, and as cement between grains within the Fo_{100} sample (Fig. 4A and D). It is possible that the volume expansion within these pre-existing fractures could propagate the fractures; however, we do not have microstructural evidence that indicates reaction-driven fracturing occurred in this sample. The composition of the magnesite along the border and within the veins is $Mg_{0.93}CO_3$, which was calculated from WDS data. WDS also indicates silica is present within the magnesite grains. The occurrence of silica most likely indicates inclusions of the amorphous silica occur within the magnesite crystal.

A mass balance calculation of the experiment indicates that the decrease in CO_2 pressure was not solely the result of carbonation. Based on the before and after water volume and sample mass, ~95% of the Fo100_s sample should have reacted. However, the mass balance calculation overestimates the amount of carbonation that actually took place. Due to the discrepancy between the mass balance calculation and the actual amount of forsterite remaining, a small CO_2 leak or small amount of water was most likely lost during the experiment. While some water may have been lost, the sample remained submerged.

The amorphous silica primarily occurs within the sample on the sides that were closest to the CO_2-water interface as a result of the tilted orientation (Fig. 5). While the precipitate does not form a defined layer, the majority of the silica occurs within ~500 μm of the edge of the sample. The amorphous silica forms grain-like shapes (Fig. 4C) that easily damage under the electron beam. Some of the grain-like amorphous silica shapes contain forsterite centers, particularly farther away from the sample edge. Except for the distinctive ~500 μm thick magnesite layer that forms a sharp boundary with the amorphous silica (Fig. 5), the magnesite and amorphous silica are rarely mixed. The orientation of this distinctive magnesite layer is parallel to the top boundary of the sample.

3.3. Fractured cylinder experiment (Fo100_f)

As the fractured Fo100 cylinder (Fo100_f) was reacted within the in-situ ^{13}C NMR probe, we observed a growth of the carbonate mineral resonance over time (Fig. 6A). Based on the size of the initial peak (~190 ppm) observed in the Fo100_s experiment, we decided to decrease the monitoring intervals to better observe the development of this carbonate-specific peak. A small broad resonance becomes evident (around ~190 ppm) after 5 days, and this feature is indicative of a CSA powder pattern that becomes increasingly intense over time. Over the duration of the reaction, an axially-symmetric carbonate CSA powder pattern becomes more apparent. No change in the solution-state bicarbonate resonance (at 161 ppm) was observed, which indicates that the system reached equilibrium with respect to pH. There was some small instrumental noise or artifacts in the 5 and 11 days spectra (Fig. 6A) that were not present in other experiments. Following the experiment, the sample was cut into two pieces along the horizontal axis. Ex-situ $^{13}C\{^1H\}$ NMR analysis used the upper portion of the sample, while the lower portion was used for thin section analysis. A fluid sample was taken of the bulk solution and analyzed by ICP-MS. Analysis of a blank experiment with a single glass tube indicates negligible concentrations of cations from the glass holder. Using the Mg concentration from the bulk solution in the Fo100_s experiment, the final

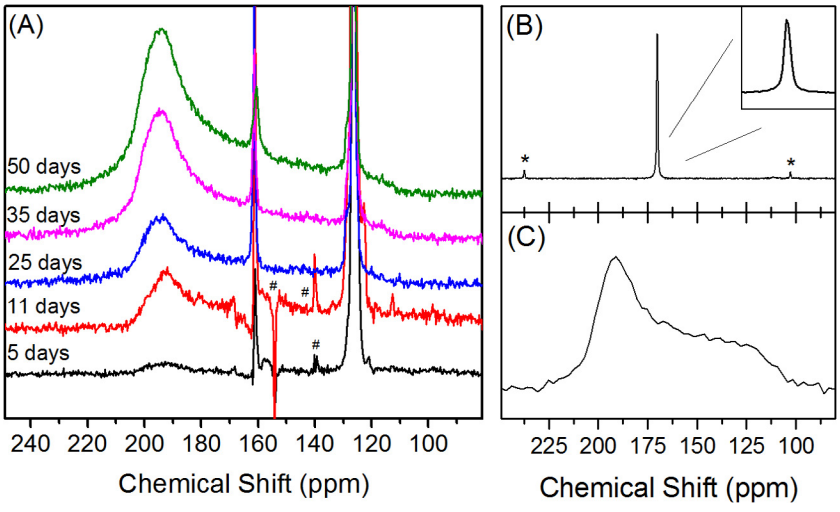

Fig. 6. ^{13}C in-situ NMR of the fractured Fo_{100} sample, Fo100_f, (A). Carbonate mineral formation is seen within 5 days of reaction time (broad peak at 190 ppm). The carbonate powder pattern continues to increase in intensity as the reaction progresses. The # symbols denote instrumental noise in the spectra. Ex-situ $^{13}C\{^1H\}$ NMR of the middle of the reacted sample are shown in (B) and (C). The MAS spectrum (B) displays a single isotropic resonance at 170.2 ppm (inset) consistent with the pure magnesite endmember. Spinning side bands are denoted with * symbols. The static $^{13}C\{^1H\}$ magnesite powder pattern of the sample is shown in (C).

pH of the bulk solution was calculated to be 5.1, which is slightly lower than the estimated pH of the Fo100_s experiment.

The ex-situ $^{13}C\{^1H\}$ MAS NMR (Fig. 6B) shows a single isotropic peak at 169.5 ppm (inset), similar to that found for the single Fo_{100} experiment (Fo100_s). This peak is also assigned to the magnesite endmember (Moore et al., 2015). The magnesite ^{13}C static powder pattern for the sample can be seen in Fig. 6C.

All sides of the Fo_{100} sample are coated in precipitates that are easily observed in optical microscopy (Fig. 7). The formation of fine particles (1–10 μm) (Fig. 7A), which are identified as magnesite using Raman spectroscopy, differs from the globular mounds we observed in the single cylinder NMR sample (Fo100_s) (Fig. 4B). The powder-like magnesite forms a ~300 μm high mound on top of a curved section and is present as a thin coat (~100 μm) along the vertical section of the sample (Fig. 7A and B). The fine magnesite grains also fill the gap between the two halves of the sample (Fig. 7A). The vertical sides and curved underside are coated in a precipitate that could not be identified with Raman spectroscopy due to high fluorescence, but was identified as magnesite using electron microscopy.

A cross-sectional analysis of the lower half of the sample shows that the thin layer (~30 μm), which was not identifiable by Raman, is composed of Cu-Zn-carbonate (Fig. 8). The copper and zinc come from the unintentional dissolution of a brass piece located near the inlet of the NMR reactor. The larger grains on the wall of the forsterite are primarily Zn-carbonates ($Zn_{0.6}Mg_{0.3}Cu_{0.1}CO_3$) (Fig. 8B). The layer then alternates between higher and lower concentrations of Cu, and it forms a sharp contact with the powder-like magnesite grains (<5 μm). Zn and Cu are not absent from the magnesite, but instead are observed in trace amounts within the magnesite grains, which have a composition of $Mg_{0.9}Cu_{0.1}CO_3$. The Cu and Zn carbonates are not limited to the wall of the sample, but are also observed in small concentrations within the sample as intergranular cement (Fig. 8C). While we observed Cu and Zn within the precipitates, concentrations of Cu^{2+} and Zn^{2+} within the bulk solution following reaction were below the ICP-MS detection limits after the reaction.

Within one side of the fractured Fo_{100} cylinder, we observe a transition from a magnesite-rich area to an amorphous silica-rich area that is oriented approximately parallel to the length of the fracture (Fig. 8). This transition is similar to the segregated precipitates we observed in the single Fo100 sample (Fo100_s; Fig. 5). Magnesite forms an intergranular cement around the host forsterite grains, only rarely as cement near amorphous silica, and is more common on the outer side of the sample (Fig. 8).

The amorphous silica is present in a thick layer (200 μm) on the fracture side (Fig. 8A) and on the side of the cylinder that was vertical and coated in the powder-like magnesite (Fig. 8A). In backscatter imaging, the amorphous silica forms grain-like structures that are similar in size and shape to the host Fo_{100} grains. Moving further from the fracture surface, the homogeneous amorphous silica layer transitions into a mix of amorphous silica with Fo_{100} centers and grains of Fo_{100} with no amorphous silica coating (Fig. 8C).

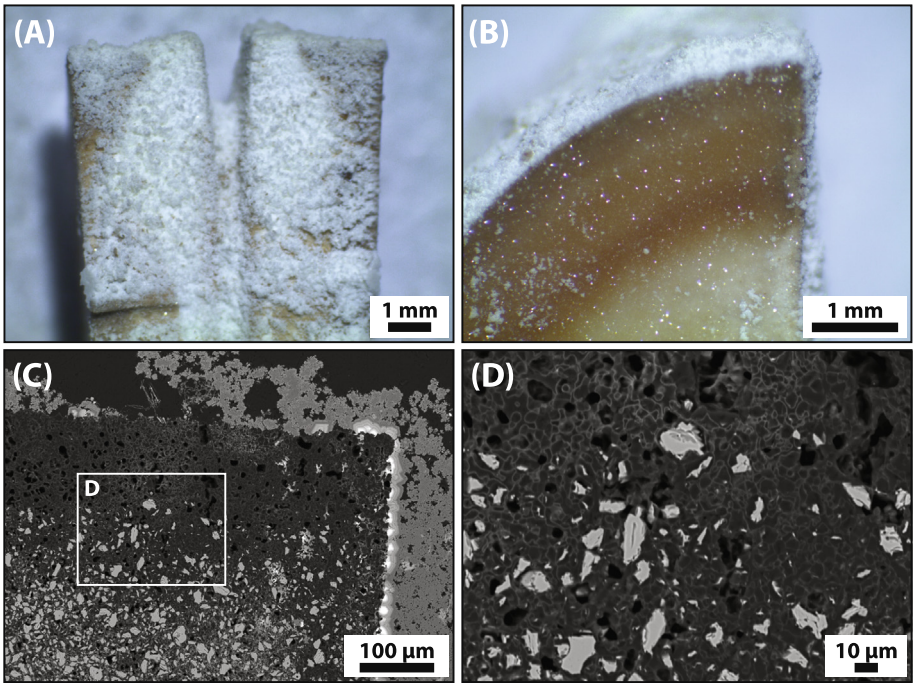

Fig. 7. Fractured Fo_{100} sample (Fo100_s) microstructures with optical photomicrographs of (A) the entire Fo_{100} sample and (B) the top portion of one half of the sample and BSE images of (C) the edge of one of the Fo_{100} pieces that is coated with a Cu-Zn carbonate; the fracture (right side) is filled with magnesite; within the sample, a 200 μm layer of amorphous silica transitions into the host Fo_{100} and (D) Fo_{100} observed at the center of amorphous silica.

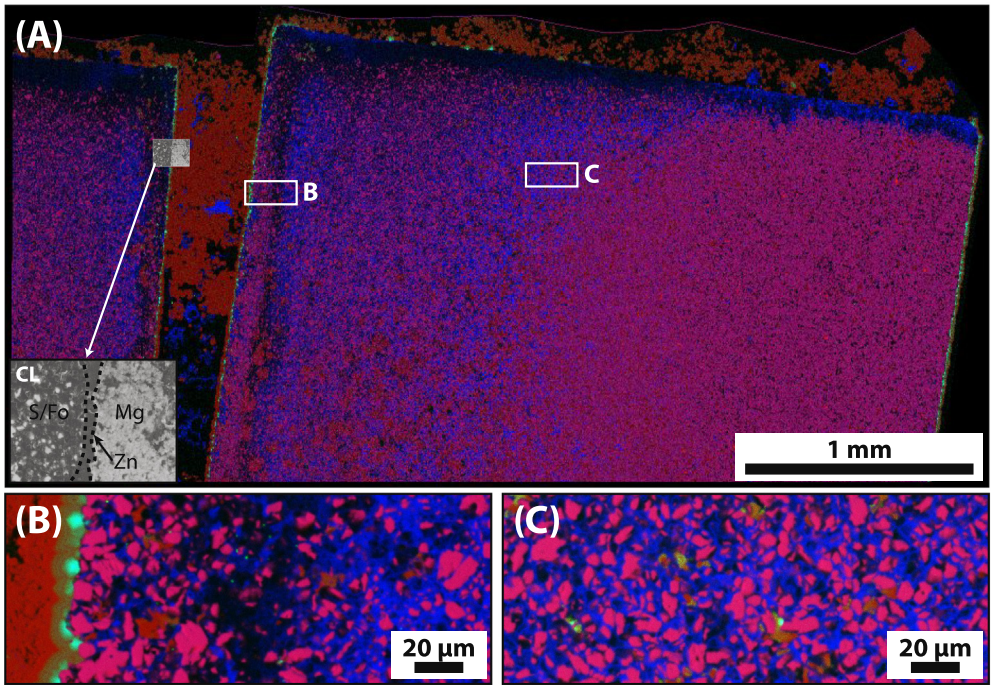

Fig. 8. Fractured Fo_{100} sample (Fo100_f) EDS maps. (A) A thin layer of copper and zinc (green) surrounds the original core. A Fo_{100}- (pink) and magnesite-rich (red) area out the outer side of the sample transitions into an area adjacent to the fracture that is now dominated by amorphous silica (purple). The vertical wall of the sample (Fig. 7A) and fracture opening are dominated by magnesite. (B) Zinc-rich carbonates form larger crystals on the sample wall and transition into magnesite. Small Fo_{100} grains are also common as cores for larger amorphous silica grains. (C) The transition zone is mixed with magnesite cement, and amorphous ringed Fo_{100}. Zn- and Cu-carbonates are also observed within the sample. Mg-red, Cu-Zn-green Si-blue. (For interpretation of the references to colour in this figure legend, the reader is referred to the web version of this article.)

4. DISCUSSION

4.1. Precipitate composition and morphology

Magnesite is observed as precipitates on the surface of the Fo_{90} and Fo_{100} reacted samples despite the different geometries, reaction times, pressure conditions, and solid-to-water ratios. Only when the reaction time is increased, as was the case for the Fo_{100}-NMR experiments, do we observe magnesite as intergranular cement and veins within the sintered samples. The biggest difference across all reacted samples in this study is the morphology of the magnesite grains. While the majority of the magnesite grains on the surface of the samples and at the bottom of the test tube are euhedral and fine grained (<100 μm), a higher density of powder-like (<5 μm) magnesite grains are observed from the fractured Fo_{100} experiment (Fo100_f) compared to the single grains that formed on all of the Fo_{90} samples and the globular mass observed in the single Fo_{100} sample (Fo100_s) The euhedral grains on the surface of every reacted sample are likely the result of crystal growth following heterogeneous nucleation, while the formation of the powder-like grains that mound on the top of the Fo_{100} sample suggest that precipitation began, at least in part, with homogeneous nucleation in solution that was followed by deposition of the magnesite particles on the cylinder surface. The powder-like carbonates are only observed in the fractured Fo_{100} experiment that had dissolved Cu^{2+} and Zn^{2+}, which was inadvertently leached from a brass piece associated with the in-situ NMR setup. The presence of Zn- and Cu-rich grains primarily on the surface of the Fo_{100} cylinder suggest the dissolved Cu^{2+} and Zn^{2+} in solution could have acted as a seed to initiate the nucleation of Zn- and Cu-rich magnesite suspended in solution and not on the Fo_{100} substrate. While seeding was not intended for this experiment, these results indicate seeding as a possible method to assist carbon storage in mafic and ultramafic reservoirs. The possibility of using metal-oxides as a catalyst for carbonation in mafic and ultramafic reservoirs is further corroborated by Wolff-Boenisch et al. (2016) who documented the development of Ni-oxide on the surface of experimentally-reacted basalt powders. While no evidence of precipitation was found, Wolff-Boenisch et al. (2016) proposed that metal-oxides might act as a nucleation site for secondary mineral precipitation, which corroborates the findings in this study.

Magnesite was the only magnesium-rich carbonate mineral observed, and no hydroxylated or hydrated magnesium carbonate minerals (i.e., nesquehonite, hydromagnesite) were observed. The reaction of Fo_{90} and Fo_{100} samples with aqueous CO_2 results in magnesite only, rather than a mixture of such species, as found previously with powdered Mg_2SiO_4 at lower temperatures (Moore et al., 2015). At lower temperatures (<100 °C) and pressures, nesquehonite

and hydromagnesite are more likely to precipitate than magnesite (Davies and Bubela, 1973; Hänchen et al., 2008; Surface et al., 2013; Qafoku et al., 2014). Xiong and Giammar (2014) documented the occurrence of hydromagnesite within 5 days of reaction using packed forsterite powder beds at 100 °C, but hydromagnesite was not observed in samples reacted for longer time periods. These observations suggest that there might also be a time component to the formation of magnesite or dehydration from hydromagnesite to magnesite. All samples within this study were reacted at 100 °C, which is more likely for magnesite precipitation, and were reacted for 15–102 days, which may have offered time for magnesite to precipitate as opposed to other kinetically slow phases.

The solubility of Zn- and Cu-rich carbonates at these conditions (100 °C, 100 bar) are more favorable for precipitation than magnesite at least in the early stages of the reaction. The initial pH of the bulk solution was calculated to be 3.2 based on the starting temperature, pressure, CO_2 solubility (Duan and Sun, 2003), and equilibrium constants of relevant acid-base reactions. While the brass piece may not have experienced that low of a pH as it was not directly in the solution, the brass with varying compositions can leach into solution at pH levels as high as 9 (Strehblow and Titze, 1980; Lytle and Schock, 1996; Badawy and Al-Kharafi, 1999). Once Cu^{2+} and Zn^{2+} dissolve into the bulk solution, the formation of Zn-rich carbonates ($ZnCO_3$; smithsonite) and Cu-rich carbonates ($Cu_3(CO_3)_2(OH)_2$; azurite) are likely to occur before the formation of magnesite. From the charge balance based on ICP-MS data and dissolved CO_2 concentration (calculated from Duan and Sun, 2003) at 100 °C, 100 bar, the pH of the final bulk solution was 5.1. The solubility product of magnesite, smithsonite, and azurite are $10^{-9.408}$, $10^{-10.752}$, and $10^{-39.726}$ (SUPCRT92), respectively. The calculated Mg^{2+}, Zn^{2+}, and Cu^{2+} concentrations needed to form magnesite, smithsonite, and azurite are 0.63, 0.029, and 0.043 mM, respectively. These calculations indicate Cu- and Zn-carbonates will form with relatively low concentrations of Cu^{2+} and Zn^{2+} in solution at these conditions compared to the higher concentration of Mg^{2+} needed to precipitate Mg-carbonates. SEM images of the fractured Fo_{100} sample indicate that the Cu- and Zn- carbonates precipitated first on the wall of the Fo_{100} cylinder based on the cross-cutting relationship with magnesite (Fig. 8). A comparison between the first appearance of bicarbonate and carbonate peaks (Figs. 3 and 6) suggests the overall reaction time was not affected by the contamination. As the reaction progresses and Mg from the Fo_{100} dissolves into solution, the calculated pH rises to 5.1 in the bulk solution based on charge balance with measured dissolved cations and calculated dissolved CO_2 (Duan and Sun, 2003). While brass becomes less reactive at higher pH levels, the formation of a passive film layer composed of $Cu(OH)_2$ on the surface of the brass piece may contribute to the decrease of Cu^{2+} and Zn^{2+} in the bulk solution (Strehblow and Titze, 1980; Badawy and Al-Kharafi, 1999). As leaching from the brass slows, the solution becomes saturated with Mg^{2+} from the Fo_{100} sample, leading to a transition from Cu- and Zn-carbonates to Mg-carbonates. Evidence of this change is observed in the 100 μm transition from the Cu- and Zn-carbonates to the magnesite. The sharp boundary between the non-luminescent Zn-Cu carbonates and the luminescent magnesite (Fig. 8A) indicates this change occurs relatively quickly.

Amorphous silica is also observed in all experiments. Amorphous silica occurred as a minor precipitate on the surface of a Fo_{90} sample (Fig. 2A) or as a thick layer that grades into the Fo_{100} sample (Figs. 5 and 8). Initial precipitation of amorphous silica probably occurs primarily on the surface of each cylinder and on the surface of Fo_{100} grains; however, when a sample is allowed to react for a longer period of time, we observe the development of a thicker amorphous silica layer as samples were reacted for longer than 15 days (Figs. 5 and 8A). These layers of amorphous silica contain grain-like structures that are either composed entirely of amorphous silica or composed of amorphous silica with Fo_{100} centers (Figs. 4C and 8B). In previous short term experiments, layers of amorphous silica observed on the surface of individual forsterite grains are thought to be the result of hydrolysis reaction with nearby silica following the dissolution of Mg^{2+} and $SiO_{2(aq)}$ from the surface of individual forsterite grains (Pokrovsky and Schott, 2000; Béarat et al., 2006; Jarvis et al., 2009; Daval et al., 2011; Olsson et al., 2012; Sissmann et al., 2013). The formation of these grain-like structures has only been documented in a few experimental studies that reacted natural peridotite in aqueous CO_2 (Hövelmann et al., 2012; van Noort et al., 2013) and olivine in a strongly acidic H_2SO_4 solution (King et al., 2011). The tendency for the amorphous silica to preserve the approximate shape of the host forsterite grain indicates that dissolution of the forsterite and precipitation of the amorphous silica occurred simultaneously and were tightly coupled at the reaction interface (Casey et al., 1993; King et al., 2011). Amorphous silica is not limited to the surface or within the Fo_{100} sample, but also occurs as angular clusters within the magnesite-filled fracture and is not associated with forsterite grains (Fig. 8A). The amorphous silica clusters that are observed within the fracture did not form there, but are clasts that exfoliated (Jarvis et al., 2009) from the amorphous silica observed on the surface of the Fo_{100} cylinder.

4.2. Analysis of post-reaction texture

A striking characteristic of the reacted Fo_{100} samples (Fo100_s and Fo100_f) in aqueous CO_2 is the formation of distinct zones of magnesite-rich areas and amorphous silica-rich zones. Similar segmented zones involving the precipitation of magnesite and amorphous silica were not observed in previous studies that reacted loose forsterite powders or single crystals (Giammar et al., 2005, 2014; Kim et al., 2005; Béarat et al., 2006; Kwak et al., 2010, 2011; Daval et al., 2011; Kwon et al., 2011; Felmy et al., 2012; Qafoku et al., 2012, 2014; Surface et al., 2013; Peuble et al., 2015); however, in powder packed bed experiments, a simple spatial distribution of magnesite precipitates with depth was observed using Raman spectroscopy and inorganic carbon analysis (Xiong and Giammar, 2014). The bulk concentration of these carbonates increases

to a maximum approximately 0.5–1 cm below the end of the bed open to well-mixed CO_2-rich solution, and then decreases along the length of the sample the longer the material is reacted (Xiong and Giammar, 2014), and this is further supported by reactive transport modeling that demonstrates an increase in the magnesite saturation index with time and a distinct location with a peak saturation index (Giammar et al., 2014). None of the prior experiments documented an organized spatial pattern involving amorphous silica beyond the tendency for it to precipitate on the surface of forsterite grains.

This study observes similar spatial trends documented in Xiong and Giammar (2014) on the vertical surface of the reacted Fo_{90} samples. The highest concentration of magnesite crystals in the zone between the surface of the Fo_{90} samples and the rubber tubing occurred approximately 1 cm below the top surface of the cylinder. This simple spatial distribution is not observed on the surface of the Fo_{100} reacted samples. Instead, we observe a thin carbonate shell that encompasses each sample and a segmented spatial distribution of precipitates beyond the surface of the sample. The higher solid-to-water ratio in the Fo_{100} experiments than in the narrow zone between the rubber tubing and the Fo_{90} cylinders more than likely influenced the timing of precipitation. A higher concentration of Mg^{2+} in the bulk solution resulted in a larger volume of precipitate that covered the entire surface of the Fo_{100} samples.

While the solid-to-water ratio certainly contributed to the timing of the carbonation, the complexity of the final precipitate structure (e.g., the amorphous silica-magnesite transition, distinct banding) that we observe in the interior of the Fo_{100} samples closely resemble textures in reacted peridotites (Andreani et al., 2009; Hövelmann et al., 2012; van Noort et al., 2013) and flow-through experiments (Peuble et al., 2015). Even though our experiments were conducted with no induced flow, we still observe these segmented zones. The development of segmented precipitates in a static environment suggests that processes other than advective flow can contribute to mobile divalent metal cations and a segregated texture. These processes may include sample-scale geochemical gradients, and complex diffusion limited zones associated with heterogeneities in the internal pore structure (e.g., pore size distribution and pore connectivity) of each sample.

Sample-scale geochemical (e.g., pH, saturation, dissolved inorganic carbon) gradients could have influenced reactions across the entire Fo_{100} sample, resulting in a spatial transition from one precipitate to another. Distinct chemical gradients several centimeters long were calculated to develop across packed powder beds (Giammar et al., 2014; Moore et al., 2015). In these models, the pH of the solution, the dissolution of the forsterite, and the saturation index of magnesite are at their lowest values towards the top of the sample, which is exposed to the bulk solution. The pH increases with depth in the packed powder beds, and a location of peak magnesite saturation occurs because of the opposing fluxes of dissolved inorganic carbon into the bed and dissolved magnesium out of the bed. Based on these calculations, a strong gradient can occur within the first 1–2 cm of the forsterite sample. It is also possible that a vertical pH gradient might have developed from the CO_2–water interface at the top of the NMR reactor to the bottom of the sample holder as the reaction progressed (Surface et al., 2013; Cui et al., 2016). The formation of vertical chemical gradients could have contributed to the sample-scale transition from amorphous silica to magnesite in the single Fo_{100} experiment, which occurred from top to bottom, with the amorphous silica-rich side closest to the spatially upward facing side closest to the CO_2–water interface. Interestingly, we also observe a horizontal sample-size gradient in each wall of the fractured Fo_{100} experiment, in which the amorphous silica-rich section developed near the narrow (<1 mm) fracture. The development of this horizontal zoning indicates the overall geometry of the reacting material may also contribute to the irregular distribution of precipitates.

Any structural heterogeneity (e.g., intergranular and interconnected porosity, fractures) of the host material may also, over time, contribute to the complexity of the texture. Preexisting pores and fractures, and the interconnection between these spaces, create zones for diffusive transport of solutes, which result in areas more favorable for magnesite precipitation. In experiments where there is no diffusion limited zones and the surface area to volume ratio is low (Giammar et al., 2005; Wolff-Boenisch et al., 2016), the time need to reach supersaturation is slow compared to samples where these zones or high surface area to volume ratios are high are present. Preferential precipitation of magnesite in our synthetic samples occurred within pores (Figs. 4D and 8C, D) and along fractures that formed during the sample preparation (Fig. 4D). Additionally, carbonates will not necessarily be limited within a fracture, but will penetrate into the fracture wall and surrounding space through available pore networks (Figs. 4D and 5). Even in environments with flow, pore spaces and terminated fractures will cause low-flow environments and diffusion-limited zones (Andreani et al., 2009; Peuble et al., 2015). As the pores and fractures are filled by precipitates, the ability of the solution to flow through the sample becomes impeded, and the reaction is limited (Hövelmann et al., 2012).

The formation of the amorphous silica layer also appears to have guided the formation of the segregated precipitate texture. In both Fo_{100} samples, the shape of the sample-scale transition is curved in relation to the amorphous silica layer (Figs. 5 and 8). Andreani et al. (2009) suggested that the development of a silica layer at the sample surface-water interface would eventually become impermeable, effectively blocking further reactions; however, in that study the layer was only a few nanometers thick. In a recent NMR study, the formation of amorphous silica did not appear to inhibit the dissolution of forsterite (Cui et al., 2016). In this study, it appears the silica layer has acted as a progressive reaction boundary that migrated inward several hundred microns, replacing the host Fo_{100} with amorphous silica. While this layer develops, magnestite precipitates away from the amorphous silica zone. The curvature associated with this layer might be more associated with a change in porosity and permeability as a result of general precipitation of amorphous silica and magnesite

than as a passivating reaction boundary. In any case, the development of the amorphous silica layer does not appear to have prevented carbonate mineral formation on or within the sample.

4.3. Implications for geologic carbon sequestration

An enticing prospect of carbon storage in fractured basalt is the possibility of mineral trapping as a permeant storage solution. In other lithologies (e.g., sandstones, carbonates, shale, coal), mineral trapping is thought to occur over thousands of years (IPCC, 2005). Based on the experiments presented in this study, the timing of carbonation of olivine-rich lithologies (e.g., peridotites) is expected to begin much earlier, particularly at higher temperatures (e.g., $\geq$100 °C). Even at lower temperatures more realistic to carbon storage (<50 °C), the mineralization of the injected CO_2 is expected to occur at faster rate compared to other reservoir types. The ability to monitor bicarbonate and carbonate formation in the in-situ NMR probe indicates that the reaction begins within a few days from the start of our experiments.

The spatial relationships of precipitates in our sintered forsterite experiments suggest that the reaction between olivine-rich lithologies and injected supercritical CO_2 may also be more complicated than in previous studies using unconsolidated particles or single grains. Despite the homogeneous mineralogy, pre-existing structural features influence the spatial progression of the reaction. Fractures will act as diffusion-limited zones, and carbonate minerals will precipitate within and into the surrounding fracture wall, guided by the intragranular porosity, while the overall shape of the fracture remains constant. While earlier studies (Béarat et al., 2006; Andreani et al., 2009; Jarvis et al., 2009; Wang and Giammar, 2013) suggest that amorphous silica may block reactive mineral surfaces and slow down subsequent reactions, the dissolution of silicate minerals may not be impeded by the formation of an amorphous silica layer. Our study indicates that this does not occur in individual grains or as a lithic unit, but rather contributes to the overall texture of the post-reaction sample. The concurrent dissolution of olivine grains and precipitation of amorphous silica results in a post-reaction sample that is not noticeably different from the starting geometry. As carbonation progresses, amorphous silica and magnesite that are already precipitated will influence the location of subsequent precipitation.

Current basalt carbon storage test sites indicate the mineralization of injected CO_2 occurs within 2 years (Matter et al., 2016; McGrail et al., 2017). While the carbonation is promising, the resulting precipitate structure may influence additional CO_2 injections or any reaction-driven fracture propagation. A heterogeneous mineralogy with different dissolution rates and more diverse carbonation reactions will influence any progressive reaction structures (e.g., the amorphous silica layer) and overall geometry of the reaction products, which may not be observed in studies of homogeneous materials. Additional studies are needed to address the influence heterogeneous compositions exert on the final reaction in natural reservoirs.

5. CONCLUSION

Magnesite and amorphous silica precipitate on the surface and within single and fractured vacuum-sintered Fo_{90} and Fo_{100} samples at 100 °C and 100 bar CO_2. In-situ NMR is a critical tool in documenting the development and timing of bicarbonate and carbonates, which occur within a few days from the start of each experiment. Compositional analysis of the reaction products found no magnesium carbonate phases (e.g., nesquehonite, hydromagnesite) other than magnesite at these high temperature conditions. Heterogeneous nucleation and crystal growth is most likely in diffusion limited zones, particularly when the reactor volume is larger. In smaller volumes (e.g., in the in-situ NMR reactor), magnesite probably formed following homogeneous nucleation within the solution, producing fine-grained carbonate particles.

Pre-existing grain boundary and pore structures, geochemical gradients, and mobile divalent metal cations contributed to the formation of a complicated post-reaction texture defined by segregated layers of magnesite and amorphous silica. While previous studies have documented preferential dissolution and precipitation in olivine and natural peridotite samples, these observations were either localized or from experiments that utilized flow-through setups. The present study observed a sample-scale texture associated with the precipitation of amorphous silica and magnesite, which developed without flow. Pre-existing structures (e.g., porosity, microfractures) therefore must act as diffusion-limited zones for carbonate precipitation. Localized precipitation of magnesite occurred within fractures and pores. The overall texture of the products is further complicated by geochemical gradients. While localized zones of amorphous silica and magnesite form as the reaction progresses, the overall shape of the material may not change as a result of balanced dissolution-precipitation reactions.

ACKNOWLEDGEMENTS

This material is based upon work supported by the Department of Energy under Award Number DE-FE0023382. The experiments with the San Carlos olivine were conducted with the support of the Consortium for Clean Coal Utilization at Washington University in St. Louis. Jill Pasteris provided valuable support of Raman analyses. Rolf Bruijn prepared the olivine sinters for the 200 mL batch experiments. Paul Carpenter provided assistance with the microprobe analyses. Additional support for electron microscopy was provided by the Institute of Materials Science and Engineering at Washington University in St. Louis. We would like to thank Domenik Wolff-Boenisch and an anonymous reviewer for their reviews of the manuscript.

REFERENCES

Andreani M., Luquot L., Gouze P., Godard M. and Gibert B. (2009) Experimental study of carbon sequestration reactions controlled by the percolation of CO_2-rich brine through peridotites. *Environ. Sci. Technol.* **43**, 1226–1231.

Badawy W. A. and Al-Kharafi F. M. (1999) Corrosion behavior of brass alloys in aqueous solutions of different pH. *Corrosion* **55**, 268–277.

Béarat H., McKelvy M. J., Chizmeshya A. V. G., Gormley D., Nunez R., Carpenter R. W., Squires K. and Wolf G. H. (2006) Carbon sequestration via aqueous olivine mineral carbonation: role of passivating sayer formation. *Environ. Sci. Technol.* **40**, 4802–4808.

Boulard E., Guyot F. and Fiquet G. (2012) The influence on Fe content on Raman spectra and unit cell parameters of magnesite – siderite solid solutions. *Phys. Chem. Miner.* **39**, 239–246.

Casey W. H., Westrich H. R., Banfield J. F., Ferruzzi G. and Arnold G. W. (1993) Leaching and reconstruction at the surfaces of dissolving chain-silicate minerals. *Nature* **366**, 253–256.

Cui J., Sesti E. L., Moore J. K., Giammar D. E. and Hayes S. E. (2016) Evidence from ^{29}Si solid-state nuclear magnetic resonance of dissolution reactions of forsterite. *Environ. Eng. Sci.*, ees.2016.0004.

Daval D., Sissmann O., Menguy N., Saldi G. D., Guyot F., Martinez I., Corvisier J., Garcia B., Machouk I., Knauss K. G. and Hellmann R. (2011) Influence of amorphous silica layer formation on the dissolution rate of olivine at 90 & #xB0;C and elevated pCO2. *Chem. Geol.* **284**, 193–209.

Davies P. J. and Bubela B. (1973) The transformation of nesquehonite into hydromagnesite. *Chem. Geol.* **12**, 289–300.

Davis M. C., Brouwer W. J., Wesolowski D. J., Anovitz L. M., Lipton A. S. and Mueller K. T. (2009) Magnesium silicate dissolution investigated by 29Si MAS, 1H–29Si CPMAS, 25Mg QCPMG, and 1H–25Mg CP QCPMG NMR. *Phys. Chem. Chem. Phys.* **11**, 6875.

Duan Z. and Sun R. (2003) An improved model calculating CO_2 solubility in pure water and aqueous NaCl solutions from 273 to 533 K and from 0 to 2000 bar. *Chem. Geol.* **193**, 257–271.

Edwards H. G. M., Villar S. E. J., Jehlicka J. and Munshi T. (2005) FT-Raman spectroscopic study of calcium-rich and magnesium-rich carbonate minerals. *Spectrochim. Acta – Part A Mol. Biomol. Spectrosc.* **61**, 2273–2280.

Felmy A. R., Qafoku O., Arey B. W., Hu J. Z., Hu M., Todd Schaef H., Ilton E. S., Hess N. J., Pearce C. I., Feng J. and Rosso K. M. (2012) Reaction of water-saturated supercritical CO_2 with forsterite: evidence for magnesite formation at low temperatures. *Geochim. Cosmochim. Acta* **91**, 271–282.

Feng J. (2009) *Intrinsic Hydrated Defects in $CaCO_3$: A Olid State NMR Spectroscopic Study*. Stony Brook University.

Franzson H., Zierenberg R. and Schiffman P. (2008) Chemical transport in geothermal systems in Iceland. Evidence from hydrothermal alteration. *J. Volcanol. Geotherm. Res.* **173**, 217–229.

Giammar D. E., Bruant R. G. and Peters C. A. (2005) Forsterite dissolution and magnesite precipitation at conditions relevant for deep saline aquifer storage and sequestration of carbon dioxide. *Chem. Geol.* **217**, 257–276.

Giammar D. E., Wang F., Guo B., Surface J. A., Peters C. A., Conradi M. S. and Hayes S. E. (2014) Impacts of diffusive transport on carbonate mineral formation from magnesium silicate-CO_2-water reactions. *Environ. Sci. Technol.* **48**, 14344–14351.

Gislason S. R. and Oelkers E. H. (2014) Carbon Storage in Basalt. *Science* **344**(80), 373–374.

Goldberg D. and Slagle A. L. (2009) A global assessment of deep-sea basalt sites for sequestration carbon. *Energy Procedia* **1**, 3675–3682.

Gribb T. T. and Cooper R. F. (1998) Low-frequency shear attenuation in polycrystalline olivine: grain boundary diffusion and the physical significance of the Andrade model for visoelastic rheology. *J. Geophys. Res.* **103**, 27267–27279.

Gudbrandsson S., Wolff-Boenisch D., Gislason S. R. and Oelkers E. H. (2011) An experimental study of crystalline basalt dissolution from 2 < pH1< 1 and temperatures from 5 to 75° C. *Geochim. Cosmochim. Acta* **75**, 5496–5509.

Hänchen M., Prigiobbe V., Baciocchi R. and Mazzotti M. (2008) Precipitation in the Mg-carbonate system-effects of temperature and CO_2 pressure. *Chem. Eng. Sci.* **63**, 1012–1028.

Hövelmann J., Austrheim H., Beinlich A. and Munz I. A. (2011) Experimental study of the carbonation of partially serpentinized and weathered peridotites. *Geochim. Cosmochim. Acta* **75**, 6760–6779.

Hövelmann J., Austrheim H. and Jamtveit B. (2012) Microstructure and porosity evolution during experimental carbonation of a natural peridotite. *Chem. Geol.* **334**, 254–265.

IPCC (2005) IPCC Special Report on Carbon Dioxide Capture and Storage. Prepared by Working Group III of the Intergovernmental Panel on Climate Change. (eds. B. Metz, O. Davidson, H. de Coninck, M. Loos, and L. Meyer), Cambridge University Press, Cambridge, United Kingdom and New York, NY, USA.

Jarvis K., Carpenter R. W., Windman T., Kim Y., Nunez R. and Alawneh F. (2009) Reaction mechanisms for enhancing mineral sequestration of CO_2. *Environ. Sci. Technol.* **43**, 6314–6319.

Kelemen P. B. and Matter J. (2008) In situ carbonation of peridotite for CO_2 storage. *Proc. Natl. Acad. Sci. U.S.A.* **105**, 17295–17300.

Kelemen P. B., Matter J., Streit E. E., Rudge J. F., Curry W. B. and Blusztajn J. (2011) Rates and mechanisms of mineral carbonation in peridotite: natural processes and recipes for enhanced, in situ CO_2 capture and storage. *Annu. Rev. Earth Planet. Sci.* **39**, 545–576.

Kim Y., Nunez R., Carpenter R. W., Chizmeshya a. V. G. and McKelvy M. J. (2005) The nanoscale mechanism for San Carlos olivine carbonation. *Microsc. Microanal.* **11**, 1530–1531.

King H. E., Plümper O., Geisler T. and Putnis A. (2011) Experimental investigations into the silicification of olivine: implications for the reaction mechanism and acid neutralization. *Am. Mineral.* **96**, 1503–1511.

Krevor S. C., Graves C. R., Van Gosen B. S. and McCafferty A. E. (2009) Delineation of magnesium-rich ultramafic rocks available for mineral carbon sequestration in the United States. *Energy Procedia* **1**, 4915–4920.

Kwak J. H., Hu J. Z., Hoyt D. W., Sears J. A., Wang C., Rosso K. M. and Felmy A. R. (2010) Metal carbonation of forsterite in supercritical CO_2 and H_2O Using solid state ^{29}Si, ^{13}C NMR spectroscopy. *J. Phys. Chem. C* **114**, 4126–4134.

Kwak J. H., Hu J. Z., Turcu R. V. F., Rosso K. M., Ilton E. S., Wang C., Sears J. A., Engelhard M. H., Felmy A. R. and Hoyt D. W. (2011) The role of H_2O in the carbonation of forsterite in supercritical CO_2. *Int. J. Greenh. Gas Control* **5**, 1081–1092.

Kwon S., Fan M., DaCosta H. F. M. and Russell A. G. (2011) Factors affecting the direct mineralization of CO_2 with olivine. *J. Environ. Sci.* **23**, 1233–1239.

Lackner K. S., Wendt C. H., Butt D. P., Joyce E. L. and Sharp D. H. (1995) Carbon dioxide disposal in carbonate minerals. *Energy* **20**, 1153–1170.

Lytle D. A. and Schock M. R. (1996) *Stagnation Time, Composition, pH, and Orthophosphate Effects on Metal Leaching from Brass. EPA/600/R*. U.S. Environmental Protection Agency, Washington, DC.

Matter J. M. and Kelemen P. B. (2009) Permanent storage of carbon dioxide in geological reservoirs by mineral carbonation. *Nat. Geosci.* **2**, 837–841.

Matter J. M., Stute M., Snæbjornsdottir S. O., Oelkers E. H., Gislason S. R., Aradottir E. S., Sigfusson B., Gunnarsson I., Alfredsson H. A., Wolff-boenisch D., Mesfin K., Dideriksen K. and Broecker W. S. (2016) Rapid carbon mineralization for permanent disposal of anthropogenic carbon dioxide emissions. *Science* **352**(80), 10–13.

McGrail B. P., Spane F. A., Sullivan E. C., Bacon D. H. and Hund G. (2011) The Wallula basalt sequestration pilot project. *Energy Procedia* **4**, 5653–5660.

McGrail B. P., Schaef H. T., Spane F. A., Cli J. B., Qafoku O., Horner J. A., Thompson C. J., Owen A. T. and Sullivan C. E. (2017) Field validation of supercritical CO2 reactivity with basalts. *Enivron. Sci. Technol. Lett.* **4**, 6–10.

Mohanan K., Sharma S. K. and Bishop F. C. (1993) A Raman spectral study of forsterite-monticellite solid solutions. *Am. Mineral.* **78**, 42–48.

Moore J. K., Surface J. A., Brenner A., Skemer P., Conradi M. S. and Hayes S. E. (2015) Quantitative identification of metastable magnesium carbonate minerals by solid-state ^{13}C NMR spectroscopy. *Environ. Sci. Technol.* **49**, 657–664.

Oelkers E. H., Gislason S. R. and Matter J. (2008) Mineral carbonation of CO_2. *Elements* **4**, 333–337.

Olsson J., Bovet N., Makovicky E., Bechgaard K., Balogh Z. and Stipp S. L. S. (2012) Olivine reactivity with CO_2 and H_2O on a microscale: implications for carbon sequestration. *Geochim. Cosmochim. Acta* **77**, 86–97.

Peuble S., Godard M., Luquot L., Andreani M., Martinez I. and Gouze P. (2015) CO_2 geological storage in olivine rich basaltic aquifers: new insights from reactive-percolation experiments. *Appl. Geochemistry* **52**, 174–190.

Pokrovsky O. S. and Schott J. (2000) Forsterite surface composition in aqueous solutions: a combined potentiometric, electrokinetic, and spectroscopic approach. *Geochim. Cosmochim. Acta* **64**, 3299–3312.

Qafoku O., Kovarik L., Kukkadapu R. K., Ilton E. S., Arey B. W., Tucek J. and Felmy A. R. (2012) Fayalite dissolution and siderite formation in water-saturated supercritical CO_2. *Chem. Geol.* **332–333**, 124–135.

Qafoku O., Hu J., Hess N. J., Hu M. Y., Ilton E. S., Feng J., Arey B. W. and Felmy A. R. (2014) Formation of submicron magnesite during reaction of natural forsterite in H_2O-saturated supercritical CO_2. *Geochim. Cosmochim. Acta* **134**, 197–209.

Schaef H. T., McGrail B. P. and Owen A. T. (2010) Carbonate mineralization of volcanic province basalts. *Int. J. Greenh. Gas Control* **4**, 249–261.

Sissmann O., Daval D., Brunet F., Guyot F., Verlaguet A., Pinquier Y., Findling N. and Martinez I. (2013) The deleterious effect of secondary phases on olivine carbonation yield: insight from time-resolved aqueous-fluid sampling and FIB-TEM characterization. *Chem. Geol.* **357**, 186–202.

Strehblow H. H. and Titze B. (1980) The investigation of the passive behaviour of copper in weakly acid and alkaline solutions and the examination of the passive film by ESCA and ISS. *Electrochim. Acta* **25**, 839–850.

Surface J. A., Skemer P., Hayes S. E. and Conradi M. S. (2013) In situ measurement of magnesium carbonate formation from CO_2 using static high-pressure and -temperature 13C NMR. *Environ. Sci. Technol.* **47**, 119–125.

Surface J. A., Wang F., Zhu Y., Hayes S. E., Giammar D. E. and Conradi M. S. (2015) Determining pH at elevated pressure and temperature using in Situ 13 C NMR. *Environ. Sci. Technol.* **49**, 1631–1638.

van Noort R., Spiers C. J., Drury M. R. and Kandianis M. T. (2013) Peridotite dissolution and carbonation rates at fracture surfaces under conditions relevant for in situ mineralization of CO_2. *Geochim. Cosmochim. Acta* **106**, 1–24.

Wang F. and Giammar D. E. (2013) Forsterite dissolution in saline water at elevated temperature and high CO_2 pressure. *Environ. Sci. Technol.* **47**, 168–173.

Wolff-Boenisch D., Galeczka I. M., Mes K. G. and Gislason S. R. (2016) A foray into false positive results in mineral dissolution and precipitation studies. *Appl. Geochem.* **71**, 9–19.

Xiong W. and Giammar D. (2014) Forsterite carbonation in zones with transport limited by diffusion. *Environ. Sci. Technol. Lett.* **1**, 333–338.

Zakharova N. V., Goldberg D. S., Sullivan E. C., Herron M. M. and Grau J. A. (2012) Petrophysical and geochemical properties of Columbia River flood basalt: implications for carbon sequestration. *Geochem. Geophys. Geosyst.* **13**, 1–22.

Associate editor: Wolfgang Bach